Solid State Ionics 340 (2019) 115020

Contents lists available at ScienceDirect

Solid State Ionics

journal homepage: www.elsevier.com/locate/ssi

Electrical properties of gadolinia doped ceria electrolytes fabricated by infiltration aided sintering

Can Sındıraç[a], Aligül Büyükaksoy[b,c], Sedat Akkurt[a,*]

[a] Izmir Institute of Technology, Department of Mechanical Engineering, Turkey
[b] Gebze Technical University, Department of Materials Science and Engineering, Turkey
[c] Gebze Technical University, Institute of Nanotechnology, Turkey

ARTICLE INFO

Keywords:
Solid oxide fuel cell
Electrolyte
Microstructure
Densification
Infiltration
Conductivity
Open circuit voltage

ABSTRACT

Common solid oxide fuel cell (SOFC) electrolyte materials (e.g., gadolinia doped ceria – GDC) demand temperatures exceeding 1400 °C for densification by conventional solid state sintering. It is very desirable to reduce the densification of the SOFC electroltytes to i) avoid microstructural coarsening of the composite anode layers, which are co-sintered with the electolyte layer in the anode supported SOFC fabrication scheme and ii) reduce energy consumption during SOFC manufacturing. We have recently demostrated a novel infiltration-aided sintering route to densify GDC ceramics at 1200 °C. In the present work, we present the electrical properties of GDC ceramics fabricated thusly. Comparison of high density (≥95%) samples fabricated by conventional or infiltration-aided sintering reveal that at 700 °C, similar total electrical conductivities are obtained, while at 300 °C, specific grain boundary resistivity is smaller in the latter. Bulk (grain) conductivity is higher in porous GDC ceramics (relative density ≤ 90%) fabricated by infiltration-aided sintering than the conventionally sintered ones with similar porosities. Finally, open circuit voltage of 0.84 V at 700 °C, obtained under dilute hydrogen and stagnant air conditions suggests that GDC ceramics densified by infiltration-aided sintering are suitable for use as SOFC electrolytes.

1. Introduction

Oxygen ion conducting ceramic electrolytes form the basis of solid oxide fuel cells (SOFCs), which are a very promising energy conversion technology, as an alternative to the conventional, combustion-based ones. Ceramic electrolytes used in SOFCs must be dense in order to deny the mixing of oxygen and fuel gases purged from the cathode and anode sides respectively and thusly avoid violent burnout and short-circuit [1–5]. An electrolyte layer with a relative density (R.D.) of ca. 95% is generally necessary to achieve a gas-tight cell [2,6].

The extensively used SOFC electrolytes such as yttria stabilized zirconia (YSZ) [5,7] and gadolinia doped ceria (GDC) [1,2,6,8] require heat treatments at relatively high temperatures ($T \geq 1400$ °C) to achieve high density via conventional solid-state sintering. The high sintering temperature of the electrolyte brings about major issues during the processing of SOFCs. For example, since the conventional anode supported SOFC fabrication method involves the co-sintering of the tape-cast anode and electrolyte layers, high sintering temperatures yield coarse anode microstructures with short triple phase boundary (TPB) lengths and thus, low electrochemical activity [9–11]. In addition, high sintering temperatures add to the manufacturing cost of SOFCs, which render these devices economically less attractive [11]. Hence, it is very desirable to reduce the sintering temperatures of SOFC electrolytes down to ≤1200 °C.

Among the possible ways to reduce the sintering temperature, the use of nano-scaled powders with extremely high surface areas is known to work well [8,12]. For example, Kleinlogel et al. obtained a relative density of 98% upon sintering the 20 nm sized-GDC powders at 1200 °C [13]. Yet, manufacturing such powders is expensive and hard to implement [12,14].

Another route to reduce the sintering temperature of SOFC electrolyte materials has been spark plasma sintering (SPS), alternatively known as field assisted sintering technique (FAST), which is based on the application of a high DC current along with uniaxial pressure, generating sparks between the particles and thus very high local temperatures [15]. However, this process is limited by the high cost of equipment required to maintain the high DC current and pressure [16].

To reduce the sintering temperature of SOFC electrolyte materials, addition of transition metal oxides (TMOs), as sintering aids has been reported in the literature. For example, to reduce the sintering

* Corresponding author.
E-mail address: sedatakkurt@iyte.edu.tr (S. Akkurt).

https://doi.org/10.1016/j.ssi.2019.115020
Received 30 May 2019; Received in revised form 2 July 2019; Accepted 2 July 2019
Available online 18 July 2019
0167-2738/

temperature of GDC, addition of CoO [17,18], CuO [18], Fe_2O_3 [19], MnO_2 [3] to initiate liquid phase sintering have been reported in the literature. Despite the achievement of RD values higher than 95% around 1100 °C [18], enhancement of the electronic conductivity of GDC which would reduce the open circuit potential of the SOFC is highly probable in the case of TMO sintering aids, due to the variable oxidation states of these additives [18,20]. Consequently, when lowering the sintering temperature of the SOFC electrolyte materials, utilization of a simple, low-cost and additive-free method is highly preferred.

As an alternative, we have recently proposed the infiltration-aided sintering method to densify the GDC electrolytes at reduced temperatures [21]. This process involves the utilization of the polymeric precursor infiltration approach, previously used to form electrocatalyst–ionic conductor composites which exhibited quite impressive electrochemical activity [22,23]. The infiltration-aided sintering, on the other hand, is performed by the infiltration of a polymeric GDC solution into a porous GDC scaffold that has been formed by partially sintering a die-pressed pellet at 1000 °C. By the infiltration process, an amorphous GDC coating on the GDC grains of the porous scaffold is formed and thus, i) partial filling of the pores prior to sintering, ii) enhancement of the coordination (i.e., number of contact points among the particles) of the GDC particles within the porous scaffold and iii) generation of a fast diffusion pathway is ensured (Fig. 1) [21]. Upon the application of a final heat treatment at temperatures as low as 1200 °C, GDC electrolytes with ca. 95% relative densities are achieved [21]. As expected, the tremendous amount of surface area provided by the nano-sized GDC infill helped boost the sintering rate early during heating. As a result of the low sintering temperatures, the dense GDC ceramics fabricated by infiltration-aided sintering had much smaller average grain size than those fabricated by conventional sintering [21]. A similar approach to the infiltration-aided sintering has also been used by Jasinski et al. [24], but to densify thin coatings of YSZ powders, which prevented detailed demonstration of densification and usability as an SOFC electrolyte. Also, only one publication reports on the electrical properties of samaria doped ceria (SDC) densified by infiltration-aided sintering [25].

In this study, the electrical properties of the GDC electrolytes fabricated by infiltration-aided sintering are investigated. More specifically, differences in the electrical conductivity, grain/grain boundary contributions to the total electrical conductivity of the GDC electrolytes fabricated by i) conventional solid-state sintering and ii) infiltration-aided sintering are determined by electrochemical impedance spectroscopy (EIS) measurements. To test the gas-tightness and thus the usability of the GDC ceramics fabricated by infiltration-aided sintering as SOFC electrolytes, open circuit voltage (OCV) measurements are also performed.

2. Experimental methods

Dense 10 mol% gadolinium-doped ceria (GDC) electrolytes were prepared by two different techniques in the present work, namely; conventional sintering and infiltration- aided sintering. The former method was based on the high-temperature firing of the consolidated (die-pressed in this case) powders, while in the latter, the die pressed powder was only partially sintered at reduced temperatures to form a porous scaffold, followed by its infiltration with polymeric GDC precursor. Then, finally, a second reduced temperature sintering process is realized. In both types of electrolytes, GDC ($Ce_{0.9}Gd_{0.1}O_{2-\delta}$, PRAXAIR > 99.9%) powders with a specific surface area of 6.5 m^2/g and a particle size distribution defined by the d_{10}, d_{50} and d_{95} values of 0.4 μm, 0.5 μm and 0.9 μm, respectively, were used to prepare the ceramic disks. The as-received powder was uniaxially pressed (Carver Hydraulic Press, Wabash, IN, USA) under 180 MPa pressure in a 15 mm diameter cylindrical stainless steel die. Afterwards, for conventional sintering, the pellets were fired in an electrically heated laboratory kiln (Nabertherm LHT 02/17, Germany) at temperatures between 1200 and 1400 °C with 8 h of soaking time. For the preparation of porous GDC scaffolds to be infiltrated with polymeric GDC precursors, the die-pressed samples were fired at 1000 °C for 6 h. In both cases, heating/cooling rate was fixed to 3 °C/min.

For the fabrication of dense GDC ceramics via infiltration-aided sintering, the porous scaffolds were loaded with GDC infiltration solution. A polymeric GDC precursor solution was used to ensure that an interconnected film, rather than disconnected precipitates on the grains of the GDC scaffold is formed.

To prepare the polymeric GDC precursor solution, $Ce(NO_3)_3.6H_2O$ (ALFA-AESAR > 99.5%) and $Gd(NO_3)_3.6H_2O$ (Sigma-Aldrich > 99.9%) salts were mixed in the $Ce_{0.9}Gd_{0.1}O_{2-\delta}$ (GDC) stoichiometry, then, dissolved in deionized water and ethylene glycol at different cation molar ratios (i.e., 0.040 to 0.080). This was followed by heating at ~80 °C until all water had evaporated. The solution was diluted with 2-butoxyethanol to ensure good wetting properties and to reduce the surface tension of polymeric solutions. This is similar to the procedure followed in our earlier work [21]. Obviously, for practical use in the industry scale, the number of infiltrations must be minimized in order to keep the process simple and quick. We believe that this is possible upon further optimization.

Fig. 1 shows schematically the infiltration process of precursor salts in porous GDC scaffold. Partially sintered porous GDC scaffold (with approximately 40% porosity) was immersed in the precursor solution in a beaker placed in a desiccator under vacuum (Lanphan 2XZ-2, Zhengzhou, Henan, China) to induce the removal of air bubbles trapped in pores and the penetration of the polymeric precursors. Afterwards, the surfaces of the pellets were wiped with a paper towel dry and heated gradually to 400 °C until all solvents and organics decomposed. This infiltration process was repeated 25 or 35 times followed by a secondary sintering process at 1000 or 1200 °C for 8 h.

In this work, for convenience, a code number was assigned to every sample. These codes and the corresponding processing steps along with RD values are summarized Table 1. For example, the sample coded as "4" indicates that porous GDC scaffold partially sintered at 1000 °C and infiltrated 25 times by a 0.040 M GDC solution. Thereafter, infiltrated pellet underwent a final sintering at 1000 °C for 8 h.

Bulk densities of the fabricated GDC ceramics pellets were measured by the Archimedes method according to ASTM C20 standard [26]. Relative densities were calculated by dividing the measured bulk

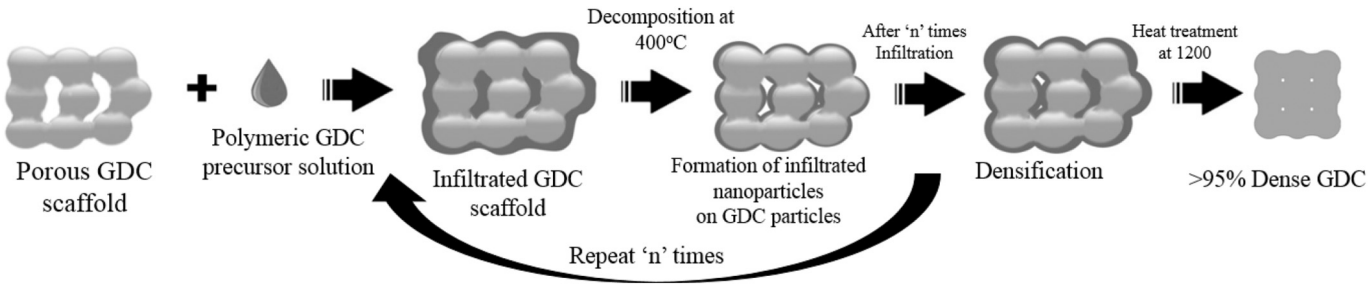

Fig. 1. Schematic representation of the infiltration-aided sintering process.

Table 1
The sample code numbers and related infiltration process parameters. Relative density and grain size values of final ceramics are also listed with the standard deviations in parenthesis. Note that 1–3 are not infiltrated.

Code number	Infiltration			Final sintering	Relative density (%)
	Number of cycles	Concentration (M)	Weight gain after infiltration but before sintering (%)	Temp. (°C)	
1	–	–	–	1200	71.8 (1.27)
2	–	–	–	1300	84.2 (0.95)
3	–	–	–	1400	97.5 (0.39)
4	25	0.040	19	1000	76.6 (2.10)
5	25	0.040	20	1200	85.6 (1.95)
6	35	0.040	27	1200	88.0 (1.80)
7	35	0.080	35	1200	95.0 (0.65)

densities by 7.2 g/cm^3 which is equal to the theoretical density of 10 mol% Gd_2O_3 doped CeO_2 [27]. While not yet measured, strengths of pellets were satisfactorily high enough to serve the purpose. Further, if this technology is applied on conventional SOFCs, they will rely on the strength provided by the supporting anode layer during operation.

The microstructural analyses of the directly-sintered and infiltration-aided sintered GDC electrolytes were performed by Scanning Electron Microscopy (SEM, Philips XL 30S FEG) utilizing secondary electron (SE) imaging. Average grain sizes of samples were determined from the SEM images of fractured surfaces of the pellets via linear intercept method as described by Mendelson [28]. More specifically, the average grain size (D) was calculated by multiplying L by 1.56 where L was the average length of several random lines drawn in measuring the grain-boundary intercept length.

For the electrochemical impedance spectroscopy (EIS) analysis, silver paste was brush-painted onto both sides of the electrolyte so that it could behave as an electrode and current collector layer. The Ag coated pellets were connected with Ag wires in alumina specimen holder inside the horizontal tubular furnace (Protherm,PTF 16/50/450, Ankara, Turkey). These cells were attached to Autolab (Metrohm) instrument to perform EIS analyses of the electrolyte in the range 250-700 °C in stagnant air with an excitation voltage amplitude of 15 mV in the frequency range 10^{-2}–10^5 Hz. Nova 2.1 software was used to fit the impedance data in Nyquist plot.

The open circuit voltage (OCV) measurements were performed at 450–700 °C using a Gamry Reference 3000 potentiostat/galvanostat/EIS analyzer (Gamry Echem Analyst). For these experiments, this time, NiO and Ag pastes were used for current collection from the fuel (a humidified mixture of 10% hydrogen – 90% argon) and air sides, respectively. The effective electrode areas were 0.5 cm^2. To ensure gas-tightness, pellets were fixed on alumina tubes by Ceramabond ceramic adhesive and glass sealant.

3. Results and discussions

Scanning electron microscopy (SEM) images of the fracture surfaces of the gadolinia doped ceria (GDC) ceramics fabricated by conventional and infiltration-aided sintering are shown in Fig. 2. Notice here that the code numbers for all seven images refer to those in Table 1. Fig. 2 (1–3) depict the SEM images of GDC samples fabricated by conventional sintering at 1200, 1300 and 1400 °C for 8 h, respectively. Evidently, increasing the temperature brings about an enhancement in the relative density (RD- Fig. 2, samples 1–3), consistent with the Archimedes measurements, which indicate an increase from 72.6% to 97% (Table 1). In the case of GDC ceramics fabricated by infiltration-aided sintering, this time, achievement of high density (RD: 95%) is possible upon heat treatment at 1200 °C (Fig. 2, sample 7). The obtained RD value increases as the number of infiltration cycles, the molarity of the infiltration solution and the secondary heat treatment temperature increases (Fig. 2, samples 4–7 and Table 1).

Although no abnormal grain growth is observed in any of the samples, the grain growth behavior differs significantly depending on the densification route (Fig. 3). The increase in RD from 71.8 to 97.5% is accompanied by an increase in the average grain size from 220 to 727 nm (Fig. 3). In the case of GDC ceramics fabricated by infiltration-aided sintering, on the other hand, the grain growth concomitant to densification is much less pronounced. Upon densification from 76.6% to 95.0% the grain size increases from 247 to only 450 nm (Fig. 3).

To determine the total electrolyte conductivity and to separate the contributions from bulk (grain) and grain boundaries to the oxygen ion transport resistance, electrochemical impedance spectroscopy is preferred in this work. The impedance spectroscopy measurements are performed on samples 1–7 at 250–700 °C, in air. For the sake of brevity, only measurements at 300 °C are shown in the Nyquist plots, in Fig. 4 which are electrolyte and electrode polarization arcs, all normalized to the electrode (current collector) area. Symbols and solid lines represent the measured data and the fitting curves, respectively. The equivalent circuit model used to perform the impedance fitting consists of one series area specific resistance (R1), corresponding to the non-zero high frequency intercept at the horizontal axis and two more area specific resistances (R2 and R3), each connected in parallel to a constant phase element (Q2 and Q3), defining the two semi-circles observed in Fig. 4.

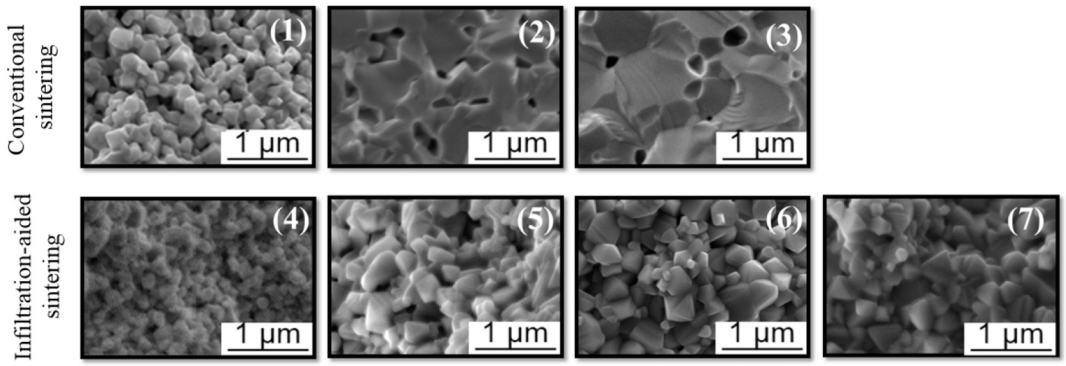

Fig. 2. Scanning electron microscopy images of the fracture surfaces of all seven samples obtained in the secondary electron mode.

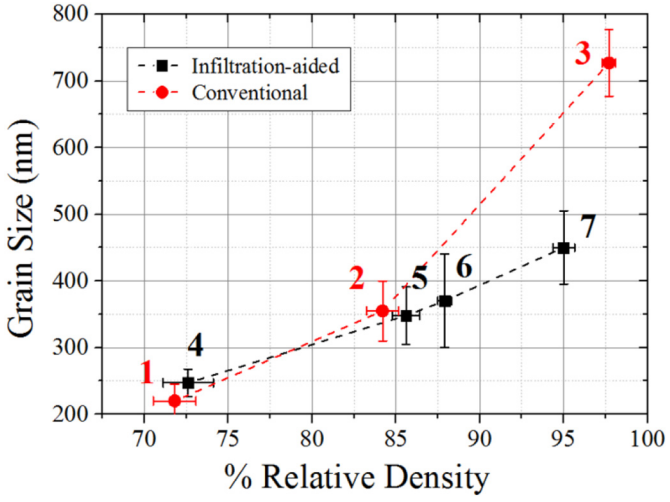

Fig. 3. Variation of grain size with relative density for all samples 1–7.

Fit lines represent the collected EIS data, which is also reflected by the χ^2 values in the range of 10^{-4} obtained in each fitting. The ASR and capacitance values obtained from the EIS fittings are given in Table 2. The capacitance and frequency values are good indicators of the electrochemical processes the resistance values correspond to [29,30]. In the present case, the capacitance values extracted from the Q2 element are in the range of 10^{-9}–10^{-10} F/cm^2, indicative of the grain boundary impedance in oxygen ion conducting ceramics [31,32]. The capacitance values in the 10^{-7}–10^{-5} F/cm^2 range suggest an electrochemical process at the Ag electrode/GDC electrolyte contact, such as oxygen reduction/evolution [31–33]. For all GDC samples, at 300 °C, the summit frequency for the bulk contribution to the ionic conduction remains higher than the maximum measurable frequency range of 10^5 Hz, and hence, this process is manifested as a series ASR in the impedance spectra (Fig. 4).

For a clear understanding of the effect of microstructure on the electrical conductivity of GDC, bulk and grain boundary resistivities (ρ_b and ρ_{gb}, respectively) are calculated via Eq. (1), where L is sample thickness, ρ and ASR are resistivity and area specific resistance respectively, both of which are applicable to bulk or grain boundary specifically.

$$\rho = \frac{ASR}{L} \tag{1}$$

Since the total resistivity (ρ_t) is the sum of bulk (ρ_b) and grain boundary resistivities (ρ_{gb}), the contribution of grain boundary resistivity to the total resistivity can be determined by $\rho_{gb}/(\rho_{gb} + \rho_b)$, variation of which depends on the grain size of the GDC ceramics fabricated by infiltration-aided sintering and conventional sintering (Fig. 5). At 300 and 350 °C and in the majority of the samples at 400 °C, the grain boundary resistivity is the dominant factor governing the total resistivity in all samples (Fig. 5a and b). The blocking effect of the grain boundaries in doped ceria has been reported in the literature extensively [3,34–38] and has been attributed to i) space charge layer formation and ii) segregation of resistive, silicous impurities therein. The prevalence of grain boundary resistivity over the total resistivity appears to be less pronounced with increasing grain size and measurement temperature (Fig. 5a-c).

In general, the effect of grain size on the $\rho_{gb}/(\rho_{gb} + \rho_b)$ value is due to the decrease in the number of grain/grain boundary interfaces that the oxygen ion needs to cross in the perpendicular direction to the grain boundary as the grain size increases, in agreement with the results observed in the literature [35,38–40]. The decrease in the $\rho_{gb}/(\rho_{gb} + \rho_b)$ value with increasing measurement temperature has also been observed in the literature [35] and implies that ion transport

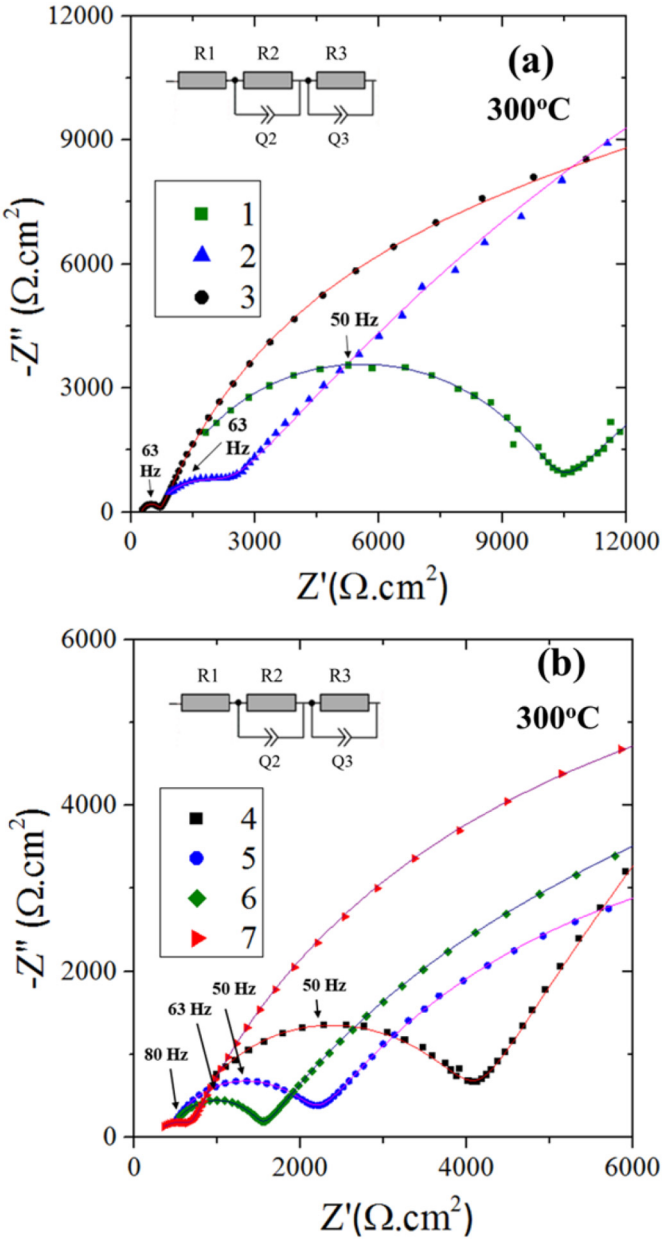

Fig. 4. High frequency portions impedance spectra measured at 300 °C for GDC fabricated by (a) conventional (b) infiltration-aided sintering along with their equivalent circuit fitting lines. The equivalent circuit models used to fit data are given as insets.

perpendicular to the grain boundary is associated with a larger activation energy than through grain.

As mentioned earlier, achievement of high density is accompanied by a significant grain growth in GDCs fabricated by conventional sintering (Sample 3), while those subjected to infiltration-aided sintering retain a microstructure with fine grains (Sample 7, Fig. 3). It is seen in Fig. 5a that, despite the significantly larger grain size in sample 3 than in sample 7, they exhibit similar $\rho_{gb}/(\rho_{gb} + \rho_b)$ values at 300 °C, i.e., in the range of 0.6, while at higher temperatures sample 7 exhibits a much lower $\rho_{gb}/(\rho_{gb} + \rho_b)$ value than does sample 3 (Fig. 5b and c). For example, at 400 °C, ρ_{gb} is no longer the larger part of $(\rho_{gb} + \rho_b)$ in sample 7, while in sample 3, this still is not the case (Fig. 5c). To analyze this finding, the specific grain boundary resistivity term (ρ_{gb}^s) is also used in the literature [34,38–42]. This term represents the inherent property of the grain boundary, free from the effects of grain boundary thickness (δ_{gb}) and grain size (d_g) as shown in Eq. (2).

Table 2
Area specific bulk (grain) and grain boundary resistances, along with the capacitance and summit frequency values extracted from the equivalent circuit fitting of the EIS data collected at 300 °C.

Code number	R1 (Ω·cm^2)	R2 (Ω·cm^2)	Capacitance from Q2 (nF)	Summit frequency (kHz)	R3 (Ω·cm^2)	Capacitance from Q3 (μF)	Summit frequency (Hz)
1	1480	19300	0.12	50	55500	0.60	1.6
2	1360	3430	0.41	63	36550	0.80	5
3	637	1110	1.35	63	13150	1.60	12
4	1140	6880	0.28	50	41200	0.55	3.1
5	924	3790	0.45	50	34960	0.72	6.3
6	939	2380	0.61	63	19560	0.95	7.9
7	678	973	1.04	80	11200	1.45	12.5

$$\rho_{gb} = \frac{\delta_{gb} \times \rho_{gb}^{s}}{dg} \quad (2)$$

When the ρ_{gb} and d_g values obtained from the experiments conducted on samples 3 and 7 are plugged into Eq. (2), ($\delta_{gb} \times \rho_{gb}^{s}$) values of 0.201 Ω.cm^2 and 0.092 Ω.cm^2 respectively are obtained at 300 °C. The reason for this difference, thus the faster decrease in the grain boundary contribution to the total resistivity in the infiltration-aided sintering case, can either be the larger grain boundary thickness or the larger specific grain boundary resistivity of the conventionally sintered GDC (Sample 3). Smaller grain size corresponds to larger grain boundary volume available to dissolve any impurities, such as SiO_2, that may cause an ion blocking effect and thus decrease ρ_{gb}^{s} [43,44]. On the other hand, since the experiments conducted in the literature on high purity ceria samples also have shown a similar effect [35,36,45], it can also be suggested that smaller grain size induces smaller δ_{gb}value, thus decreasing the overall ρ_{gb}. However, it should be noted that the determination of the exact δ_{gb} value is certainly not straightforward due to the presence of space charge effect, even with high resolution transmission electron microscopy analyses [35].

Temperature dependence of bulk and grain boundary conductivities (σ_b and σ_{gb}, respectively), determined by taking the reciprocals of ρ_{gb} and ρ_b respectively, of GDC ceramics fabricated by conventional and infiltration-aided sintering are given in Fig. 6. Since at temperatures exceeding 425 °C, distinguishing the bulk and grain boundary contributions is practically not possible for GDC (as also was the case in Refs [8,30,46]), these measurements were collected at 250–400 °C in 25 °C intervals, in air. To determine the effects of grain size on σ_b, samples fabricated by the two methods mentioned here having similar densities must be compared. This comparison yields that GDC ceramics fabricated by infiltration-aided sintering exhibit higher σ_b than the conventionally sintered ones at RDs below ca. 90%, despite similar densities and grain sizes while similar σ_b values are obtained in samples with RDs exceeding 95% regardless of the grain size (Fig. 5a). For

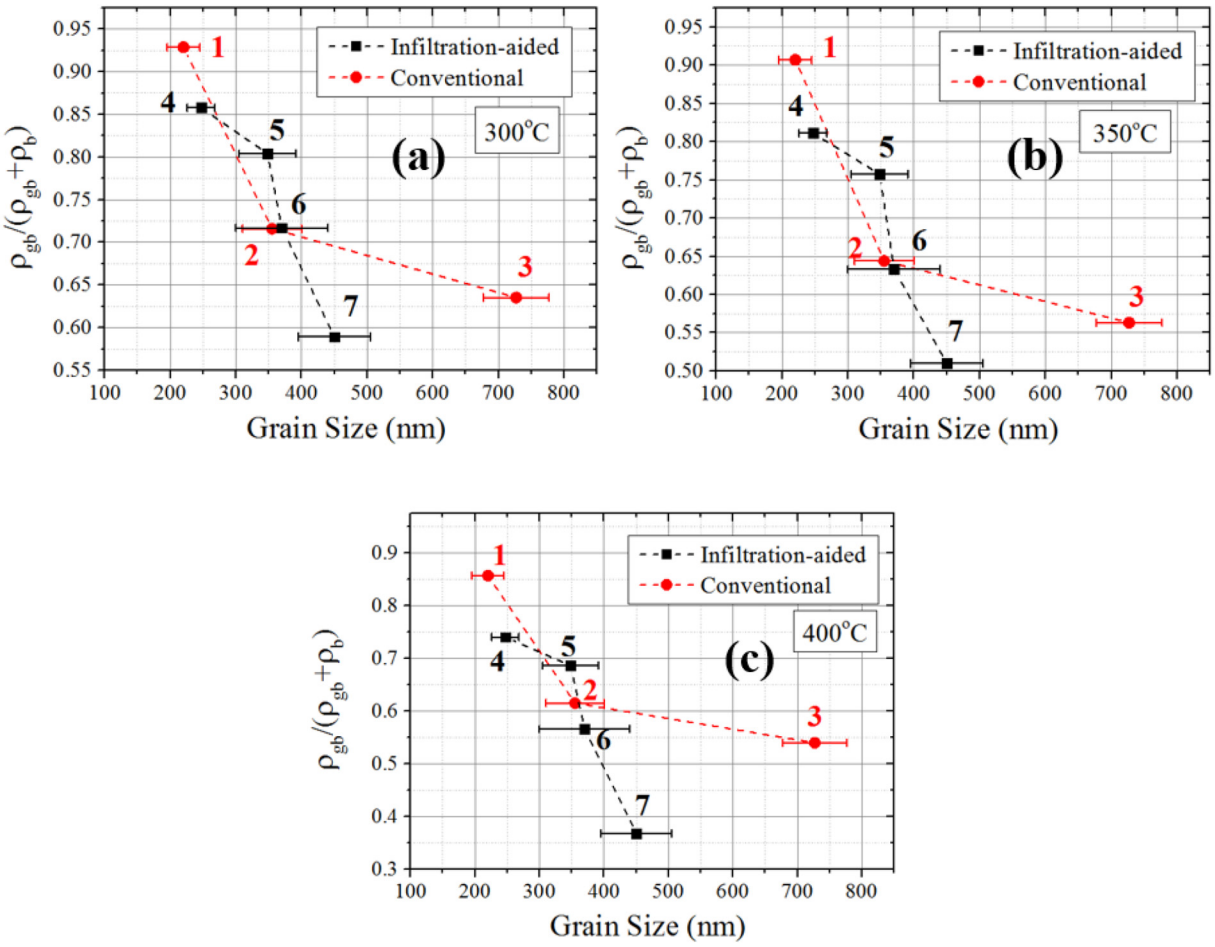

Fig. 5. Effect of grain size on the ratio of grain boundary resistivity to total resistivity as measured at (a) 300, (b) 350 and (c) 400 °C.

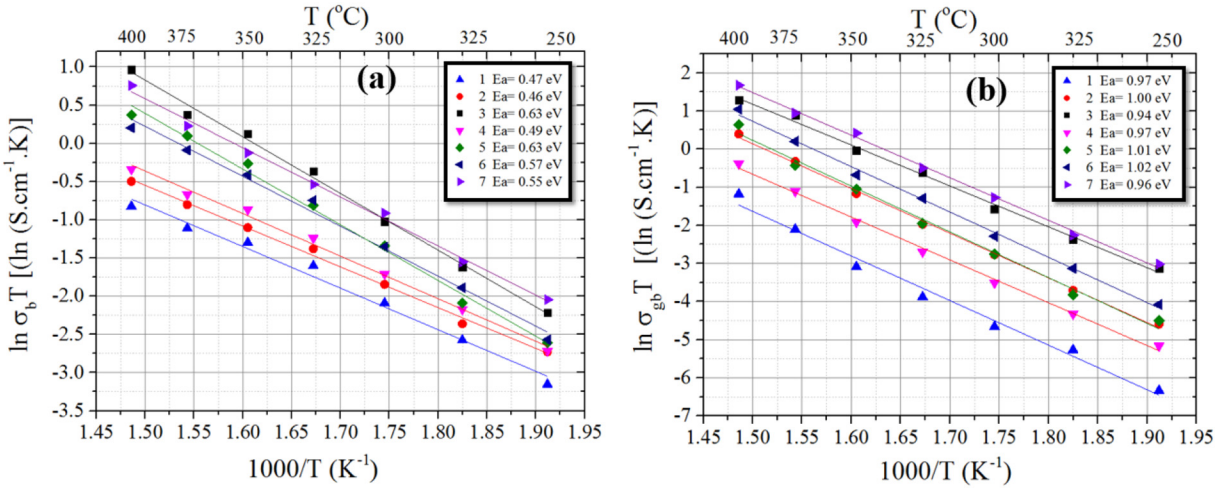

Fig. 6. Arrhenius plots of (a) bulk (grain) and (b) grain boundary conductivities of the seven samples and their activation energies.

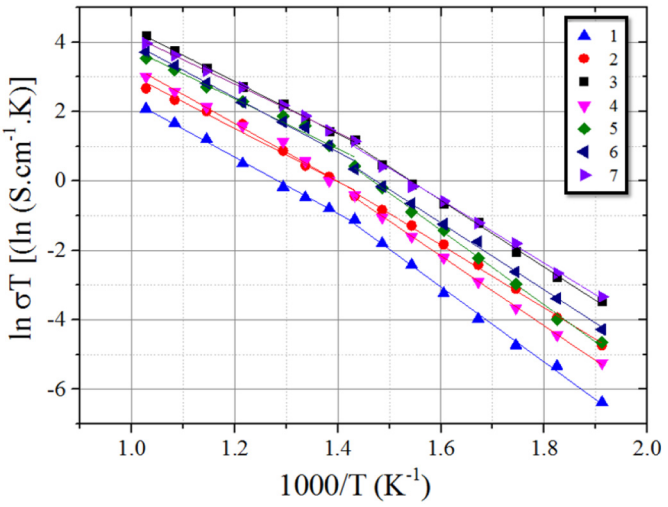

Fig. 7. Temperature dependences of the total conductivities of all samples and their activation energies.

example, although samples 1 and 4, and samples 2 and 5 have similar densities and grain sizes (Fig. 3), those fabricated by infiltration-aided sintering exhibit higher σ_b values (i.e., samples 4 and 5 have higher σ_b than samples 1 and 2) as seen in Fig. 6a. On the other hand, samples 5 and 6 (both fabricated by infiltration-aided sintering) exhibit similar σ_b values (Fig. 6a) and are determined to have similar densities and grain sizes (Fig. 3). The comparison of the two high density samples (RDs exceeding 95%) fabricated by the two different methods discussed here (samples 3 and 7) yields similar σ_b values (Fig. 6a) despite their significantly different grain sizes (Fig. 3). A possible explanation is that in the case of infiltration-aided sintering, the number of coordination among the GDC particles constituting the porous scaffold is enhanced by the polymeric GDC precursor infiltration without a significant increase in RD, as suggested in Ref 21, causing an increase in the measured σ_b value. This argument is supported by the fact that no such difference in σ_b is observed between samples 5 and 6 – samples fabricated by infiltration-aided sintering with similar densities and grain sizes. In the case of samples with RDs exceeding 95%, the σ_b values are similar because the coordination between the GDC particles is at their maximum value in both cases.

A comparison among the σ_b values of GDC ceramics fabricated by the same method (i.e., conventional or infiltration aided sintering) suggests that bulk conductivity increases with increasing density (Fig. 6a) as also reported in the literature [35,47,48]. In addition, grain boundary conductivities (σ_{gb}) also appear to be affected by this parameter (Fig. 6b). This apparent effect is due to the higher effective amounts of material within the measurement sample and, as discussed earlier in terms of specific grain boundary resistivity (ρ_{gb}^{s}) values of the highest density samples, ion transport perpendicular to the grain boundary appears to be more facile in the case of smaller grain size.

As all samples exhibit Arrhenius-type behaviors, the determination of activation energy (Ea) values is realized via Eq. (3).

$$\sigma T = \sigma_0 \exp\left(\frac{-Ea}{kT}\right) \quad (3)$$

Here, σ is conductivity, Ea is the activation energy, σ_0 is the pre-exponential factor, T is the absolute temperature and k is the Boltzman's constant. Regardless of the fabrication method, density or grain size, the Ea values for bulk conductivity lie in the 0.49–0.65 eV range (Fig. 6a inset), while those for the grain boundary conductivity vary between 0.94 and 0.99 eV (Fig. 6b inset). In general, these values explain the decrease in $\rho_{gb}/(\rho_{gb}+\rho_b)$ with increasing temperature (Fig. 5a-c) and are consistent with those reported in the literature [39,49–51]. In the literature, the reason for the higher activation energies observed for grain boundary conductivity in comparison to those determined for the bulk conductivity has been attributed both to the siliceous impurity segregation [37,45] and to the presence of a space charge layer at the grain boundaries [34,35].

Fig. 7 shows the temperature dependences of total conductivities of GDC ceramics fabricated by conventional and infiltration-aided sintering in the temperature range of 250 to 700 °C, in air. A significant decrease in the slope of the electrical conductivity is observed in all samples at around 425 °C (Fig. 7). A possible explanation of this phenomenon may be that since at low temperatures ρ_{gb} is dominant over ρ_b, the higher Ea value of the former prevails. On the other hand at higher temperatures, ρ_b with the lower Ea predominates. However, this argument is negated by the fact that ρ_{gb} is dominant in $(\rho_{gb}+\rho_b)$ by a small margin at 300 °C, which ceases to exist at ≥350 °C for samples 3 and 7, whereas these samples exhibit a change in the Ea of the total conductivity at much higher temperatures of 425 °C (Fig. 7).

This change in slope has also been reported in the literature and has been attributed to the presence of associated ($Gd_{Ce}^{'}$- $V_o^{\cdot\cdot}$) complexes at lower temperatures, which require extra energy to be dissociated and thusly provide available charge carriers for oxygen ion conduction [6,52]. On the other hand, at higher temperatures, these associated defects are already dissociated and the observed Ea is directly related to the migration energy of the oxygen ions [35,52,53]. Therefore, the differences in activation energies in high and low temperature ranges provide the association energies of the complexes (i.e. $Gd_{Ce}^{'}$- $V_o^{\cdot\cdot}$) [6].

Table 3
Variation of activation energy of total electrical conductivity in the lower and higher temperature range. T* refers to the transition temperature and is 425 °C for all samples in the present case.

Sample code	Ea at T < T*	Ea at T > T*
1	0.93	0.70
2	0.82	0.67
3	0.83	0.65
4	0.89	0.72
5	0.87	0.68
6	0.83	0.64
7	0.78	0.61

This energy value does not appear to be affected by the densification method, but rather a gradual decrease with increasing density is observed (Table 3). The association energy values obtained for the highest density samples, i.e., samples 3 and 7 are found as 0.16 and 0.15 eV, respectively, agreeing well with the previous works of Steele et al. (0.13 eV) [6], Zhou et al. (0.12 eV) [35] and Huang et al. (0.16 eV) [54].

Regardless of the fabrication method, electrical conductivities at 600 and 700 °C increase with increasing relative density, as expected (Fig. 8a and b). The samples with RD values exceeding 95% obtained by conventional and infiltration-aided sintering (samples 3 and 7, respectively) exhibit very similar electrical conductivities over the whole temperature range (Fig. 7). More specifically, at the targeted SOFC operation temperature of 700 °C, the GDC ceramics fabricated by conventional and infiltration-aided sintering has electrical conductivities of 0.068 and 0.054 S/cm, respectively (Fig. 8b). These values are also in the range of what has been reported in the literature for dense GDC ceramics [6,35,49,55]. This suggests that, by infiltration-aided sintering, the sintering temperatures of GDC ceramics can be reduced by ca. 200 °C, without compromising electrical conductivity.

In the case of lower density samples, those fabricated by infiltration-aided sintering appear to exhibit higher total electrical conductivity in general (Fig. 8), likely related to the higher number of coordination among the GDC particles ensured by the polymeric GDC precursor infiltration [21].

So far, infiltrated GDC electrolytes sintered at 1200 °C are shown to be highly dense and to perform well as far as their electrical conductivities are concerned. However, in addition to sufficient ionic conductivity, a suitable SOFC electrolyte material must also be impervious to hydrogen and oxygen gases at the desired operating temperatures and exhibit high open circuit voltage (OCV). Therefore, to further demonstrate the usefulness of the infiltration-aided sintering technique for SOFC electrolyte fabrication, OCV measurements are

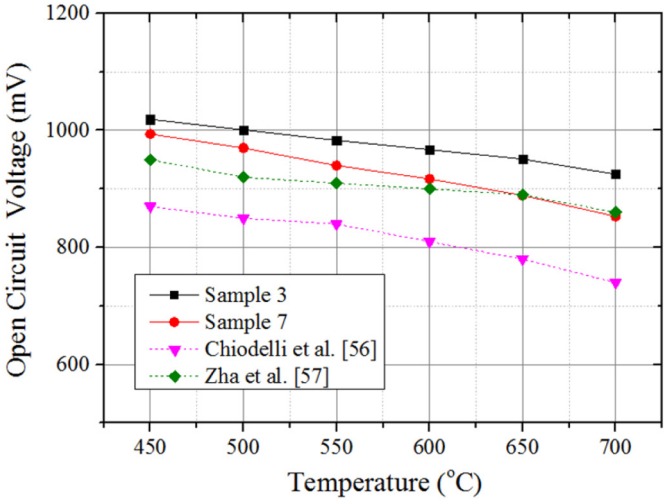

Fig. 9. Open circuit voltage values obtained under stagnant air and 10% hydrogen – 90% argon at the cathode and anode sides respectively, at 450–700 °C in samples 3 and 7. Dotted lines are obtained from refs [56, 57].

conducted on samples coded 3 and 7 between 400 and 700 °C under a humidified 10% hydrogen – 90% argon gas flow from the anode side and stagnant air conditions at the cathode side. In addition to these two samples, data from the literature are also included in the plots for comparison [56,57]. As can be seen in Fig. 9, for both samples, OCV is highest around 450 °C and gradually decreases with increasing temperature, as predicted by the Nernst Equation. At the targeted SOFC operating temperature of 700 °C, the conventionally sintered, dense GDC ceramic exhibits OCV values of 0.92 V, while that fabricated by infiltration-aided sintering yields an OCV of 0.83 V. These values are close to what has been reported in the literature for dense GDC ceramics and are well in the acceptable range for SOFC applications.

4. Conclusions

Reducing the densification temperatures of solid oxide fuel cell (SOFC) electrolyte materials is very desirable in order to i) avoid the coarsening of the anode microstructure, which is sintered together with the electrolyte layer in the anode supported SOFC fabrication scheme and ii) reduce energy consumption when manufacturing SOFCs. Our recent studies have shown that, using an infiltration-aided sintering method, the widely used gadolinia doped ceria (GDC) electrolyte ceramics could be densified up to a relative density (RD) of 95% at temperatures ca. 200 °C lower than those used in conventional sintering

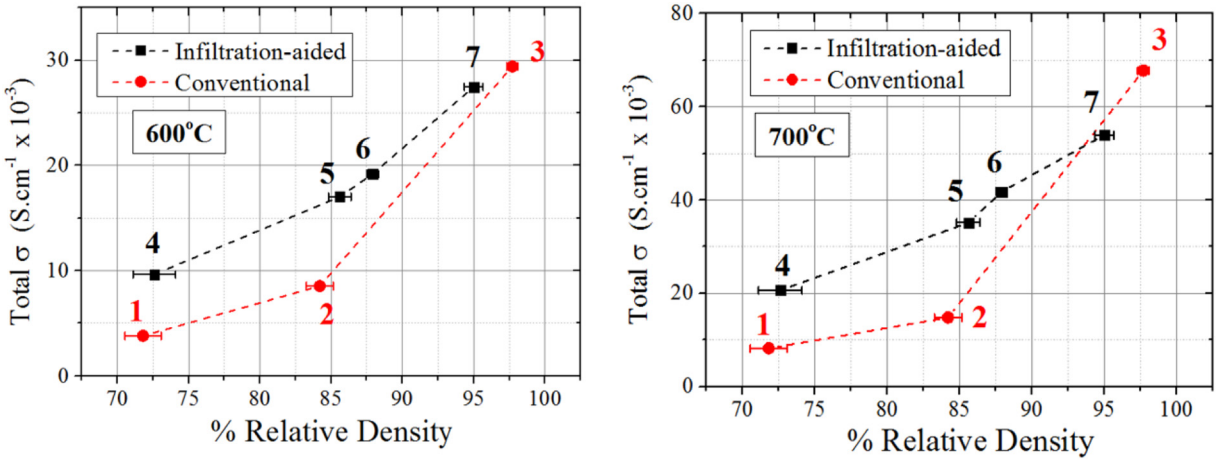

Fig. 8. Variation of total electrical conductivity with relative density for all samples.

[21]. Achievement of high density in the GDC ceramics fabricated by infiltration-aided sintering was not accompanied by significant grain growth, unlike the case of conventional sintering. In this work, we have studied the electrical properties of the GDC ceramics fabricated by infiltration-aided and conventional sintering method.

Regardless of the fabrication method, at 300 and 350 °C, grain boundary resistivity dominated the total resistivity (i.e., $\rho_{gb} / (\rho_{gb} + \rho_b)$ value which ranged between 0.5 and 1.0), which became less pronounced with increasing grain size and temperature, due to the smaller number of grain boundaries perpendicular to the oxygen ion motion and the higher activation energy of the oxygen ion transport therein. This dominance ceased to exist at 450 °C and at grain sizes of 450 nm in samples prepared by infiltration-aided sintering, but not in those fabricated by conventional sintering, even at a grain size of 727 nm, suggesting a higher specific grain boundary resistivity – grain boundary thickness product ($\delta_{gb} \times \rho_{gb}^{s}$) in the former.

It was found that, regardless of the fabrication method, the grain boundary conductivities increased with increasing grain size, as expected. The grain conductivity of the ceramics fabricated by infiltration-aided sintering was larger in samples with < 90% RD, due possibly to the enhanced coordination among the GDC particles that make up the porous GDC scaffold upon polymeric GDC precursor infiltration. This was also the case in the total electrical conductivity measurements. However, samples with RDs ≥95%, the maximum coordination of particles had been achieved, thus, similar bulk and total conductivity values were obtained.

In order to further demonstrate the usability GDC ceramics fabricated by the infiltration-aided sintering method as SOFC electrolytes, open circuit voltage (OCV) measurements were performed at 400–700 °C, under humidified 10% hydrogen – 90% argon and stagnant air atmospheres from anode and cathode sides respectively. OCV values of 0.84 and 0.93 V obtained from dense GDC ceramics fabricated by infiltration-aided and conventional sintering, respectively, suggests that the former method is also suitable for SOFC electrolyte fabrication.

Acknowledgements

This project is supported by TUBITAK (The Scientific Research Council of Turkey) through project no. 116R072. Authors would like to thank different labs in both Izmir Institute of Technology and Gebze Technical University for their helps in materials characterization.

References

[1] H. Inaba, T. Nakajima, H. Tagawa, Solid State Ionics 106 (1998) 263.
[2] H. Inaba, H. Tagawa, Solid State Ionics 83 (1) (1996).
[3] A. Horovistiz, R. Rocha, E. Muccillo, Ceram. Int. 39 (5) (2013) 5887–5892.
[4] N.Q. Minh, J. Am. Ceram. Soc. 76 (3) (1993) 563–588.
[5] T. Tsai, S.A. Barnett, Journal of Electrochemical Society 145 (5) (1998) 1696.
[6] B.C.H. Steele, Solid State Ionics 129 (2000) 95–110.
[7] A.J. Flegler, T.E. Burye, Q. Yang, J.D. Nicholas, Ceram. Int. 40 (10) (2014) 16323–16335.
[8] M. Rahaman, Y. Zhou, J. Eur. Ceram. Soc. 15 (10) (1995) 939–950.
[9] W. Bao, Q. Chang, G. Meng, J. Membr. Sci. 259 (1–2) (2005) 103–109.
[10] A. Masini, T. Strohbach, F. Šiška, Z. Chlup, I. Dlouhý, Materials 12 (2) (2019) 306.
[11] X.-V. Nguyen, C.-T. Chang, G.-B. Jung, S.-H. Chan, W. Huang, K.-J. Hsiao, W.-T. Lee, S.-W. Chang, I.-C. Kao, Energies 9 (9) (2016) 701.
[12] C. Kleinlogel, L.J. Gauckler, Adv. Mater. 13 (14) (2001) 1081–1085.
[13] C. Kleinlogel, L.J. Gauckler, Solid State Ionics 135 (2000) 567.
[14] S. Taub, R.E. Williams, X. Wang, D.W. Mccomb, J.A. Kilner, A. Atkinson, Acta Mater. 81 (2014) 128–140.
[15] L. Spiridigliozzi, M. Biesuz, G. Dell'Agli, E.D. Bartolomeo, F. Zurlo, V.M. Sglavo, J. Mater. Sci. 52 (12) (2017) 7479–7488.
[16] M. Biesuz, V.M. Sglavo, J. Eur. Ceram. Soc. 39 (2–3) (2019) 115–143.
[17] C. Kleinlogel, L.J. Gauckler, J. Electroceram. 5 (3) (2000) 231–243.
[18] D.P. Fagg, V.V. Kharton, J.R. Frade, J. Electroceram. 9 (2002) 199–207.
[19] T.S. Zhang, J. Ma, L.B. Kong, S.H. Chan, P. Hing, J.A. Kilner, Solid State Ionics 167 (2004) 203–207.
[20] C. Zhang, J. Sunarso, Z. Zhu, S. Wang, S. Liu, Solid State Ionics 310 (2017) 121–128.
[21] C. Sındıraç, S. Çakırlar, A. Büyükaksoy, S. Akkurt, J. Eur. Ceram. Soc. 39 (2–3) (2019) 409–417.
[22] J.M. Vohs, R.J. Gorte, Adv. Mater. 21 (9) (2009) 943–956.
[23] S.P. Jiang, Int. J. Hydrog. Energy 37 (2012) 449–470.
[24] P. Jasinski, V. Petrovsky, T. Suzuki, T. Petrovsky, H.U. Anderson, J. Electrochem. Soc. 152 (2) (2005).
[25] P. Jasinski, Solid State Ionics 177 (26–32) (2006) 2509–2512.
[26] ASTM, C20–00(2015), Standard Test Methods for Apparent Porosity, Water Absorption, Apparent Specific Gravity, and Bulk Density of Burned Refractory Brick and Shapes by Boiling Water, ASTM International, West Conshohocken, PA, 2015www.astm.org.
[27] M. Chourashiya, J. Patil, S. Pawar, L. Jadhav, Mater. Chem. Phys. 109 (1) (2008) 39–44.
[28] M.I. Mendelson, J. Am. Ceram. Soc. 52 (8) (1969) 443–446.
[29] X. Guo, R. Waser, Prog. Mater. Sci. 51 (2) (2006) 151–210.
[30] K. Anjaneya, G. Nayaka, J. Manjanna, G. Govindaraj, K. Ganesha, J. Alloys Compd. 578 (2013) 53–59.
[31] D. Pérez-Coll, D. Marrero-López, P. Núñez, S. Piñol, J. Frade, Electrochim. Acta 51 (28) (2006) 6463–6469.
[32] M. Gerstl, E. Navickas, G. Friedbacher, F. Kubel, M. Ahrens, J. Fleig, Solid State Ionics 185 (1) (2011) 32–41.
[33] K. Anjaneya, G. Nayaka, J. Manjanna, G. Govindaraj, K. Ganesha, J. Alloys Compd. 578 (2013) 53–59.
[34] X. Guo, W. Sigle, J. Maier, J. Am. Ceram. Soc. 86 (1) (2003) 77–87.
[35] X.-D. Zhou, W. Huebner, I. Kosacki, H.U. Anderson, J. Am. Ceram. Soc. 85 (7) (2004) 1757–1762.
[36] A. Tschope, S. Kilassonia, R. Birringer, Solid State Ionics 173 (1–4) (2004) 57–61.
[37] D.Y. Wang, A. Nowick, J. Solid State Chem. 35 (3) (1980) 325–333.
[38] H.J. Avila-Paredes, K. Choi, C.-T. Chen, S. Kim, J. Mater. Chem. 19 (27) (2009) 4837.
[39] Z. Wang, G.M. Kale, X. Tang, J. Mater. Sci. 49 (8) (2014) 3010–3015.
[40] K.-R. Lee, J.-H. Lee, H.-I. Yoo, J. Eur. Ceram. Soc. 34 (10) (2014) 2363–2370.
[41] D.K. Kim, P.-S. Cho, J.-H. Lee, D.-Y. Kim, H.-M. Park, G. Auchterlonie, J. Drennan, Electrochem. Solid-State Lett. 10 (5) (2007).
[42] J.-H. Lee, T. Mori, J.-G. Li, T. Ikegami, M. Komatsu, H. Haneda, J. Electrochem. Soc. 147 (7) (2000) 2822.
[43] M.C. Martin, M.L. Mccartney, Solid State Ionics 161 (2003) 67–79.
[44] M. Verkerk, B. Middelhuis, A. Burggraaf, Solid State Ionics 6 (2) (1982) 159–170.
[45] R. Gerhardt, A.S. Nowick, J. Am. Ceram. Soc. 69 (9) (1986) 641–646.
[46] M. Chourashiya, J. Patil, S. Pawar, L. Jadhav, Mater. Chem. Phys. 109 (1) (2008) 39–44.
[47] E.C.C. Souza, W.C. Chueh, W. Jung, E.N.S. Muccillo, S.M. Haile, J. Electrochem. Soc. 159 (5) (2012).
[48] A. Hara, Y. Hirata, S. Sameshima, N. Matsunaga, T. Horita, J. Ceram. Soc. Jpn. 116 (1350) (2008) 291–297.
[49] K.R. Reddy, K. Karan, J. Electroceram. 15 (1) (2005) 45–56.
[50] W.J. Bowman, J. Zhu, R. Sharma, P.A. Crozier, Solid State Ionics 272 (2015) 9–17.
[51] G.M. Christie, F.P.F. van Berkel, Solid State Ionics 83 (1996) 17.
[52] S. Ramesh, K.C. Raju, J. *Electrochemical and Solid-State Letters* 15 (3) (2012).
[53] C. Zhang, C.-J. Li, G. Zhang, X.-J. Ning, C.-X. Li, H. Liao, C. Coddet, Mater. Sci. Eng. B 137 (1–3) (2007) 24–30.
[54] K. Huang, M. Feng, J.B. Goodenough, J. Am. Ceram. Soc. (1998) 357–362.
[55] A.V. Coles-Aldridge, R.T. Baker, Solid State Ionics 316 (2018) 9–19.
[56] G. Chiodelli, L. Malavasi, Ionics 19 (8) (2013) 1135–1144.
[57] S. Zha, C. Xia, G. Meng, J. Power Sources 115 (1) (2003) 44–48.